Nuclear Instruments and Methods in Physics Research A 660 (2011) 121–129

Contents lists available at SciVerse ScienceDirect

Nuclear Instruments and Methods in Physics Research A

journal homepage: www.elsevier.com/locate/nima

Automated segmentation of synchrotron radiation micro-computed tomography biomedical images using Graph Cuts and neural networks

Anderson Alvarenga de Moura Meneses [a,*], Alessandro Giusti [b], André Pereira de Almeida [c], Liebert Parreira Nogueira [c], Delson Braz [c], Regina Cely Barroso [d], Carlos Eduardo deAlmeida [a]

[a] Radiological Sciences Laboratory, Rio de Janeiro State University, Rua São Francisco Xavier 524, CEP 20550-900, RJ, Brazil
[b] IDSIA (Dalle Molle Institute for Artificial Intelligence), University of Lugano, Switzerland
[c] Nuclear Engineering Program, Federal University of Rio de Janeiro, RJ, Brazil
[d] Laboratory of Applied Physics on Biomedical Sciences, Physics Department, Rio de Janeiro State University, RJ, Brazil

ARTICLE INFO

Article history:
Received 12 February 2011
Received in revised form
1 August 2011
Accepted 3 August 2011
Available online 11 August 2011

Keywords:
Synchrotron radiation
Phase contrast imaging
micro-Computed Tomography
Image segmentation
Energy minimization via Graph Cuts
Artificial neural networks

ABSTRACT

Synchrotron Radiation (SR) X-ray micro-Computed Tomography (μCT) enables magnified images to be used as a non-invasive and non-destructive technique with a high space resolution for the qualitative and quantitative analyses of biomedical samples. The research on applications of segmentation algorithms to SR-μCT is an open problem, due to the interesting and well-known characteristics of SR images for visualization, such as the high resolution and the phase contrast effect. In this article, we describe and assess the application of the Energy Minimization via Graph Cuts (EMvGC) algorithm for the segmentation of SR-μCT biomedical images acquired at the Synchrotron Radiation for MEdical Physics (SYRMEP) beam line at the Elettra Laboratory (Trieste, Italy). We also propose a method using EMvGC with Artificial Neural Networks (EMANNs) for correcting misclassifications due to intensity variation of phase contrast, which are important effects and sometimes indispensable in certain biomedical applications, although they impair the segmentation provided by conventional techniques. Results demonstrate considerable success in the segmentation of SR-μCT biomedical images, with average Dice Similarity Coefficient 99.88% for bony tissue in Wistar Rats rib samples (EMvGC), as well as 98.95% and 98.02% for scans of *Rhodnius prolixus* insect samples (Chagas's disease vector) with EMANNs, in relation to manual segmentation. The techniques EMvGC and EMANNs cope with the task of performing segmentation in images with the intensity variation due to phase contrast effects, presenting a superior performance in comparison to conventional segmentation techniques based on thresholding and linear/nonlinear image filtering, which is also discussed in the present article.

1. Introduction

Synchrotron Radiation (SR) [1] facilities provide high brilliance X-rays with very high flux at small source size compared to tube X-rays, enabling investigations of samples in the micro- and even the sub-micrometer levels. Therefore micro-Computed Tomography (μCT) [2] obtained with SR X-ray conjugates several qualities for the investigation of biomedical structures such as high brilliance and high space resolution. Besides the characteristics resulting from the high coherence and monochromaticity of the beam, it is also possible to achieve the enhancing of contrast during imaging due to wavefield phase information, when absorption effects do not provide sufficient information to distinguish structures in, for example, media with low density, such as soft tissue or insects' biological structures. This interesting specificity of the SR, the *phase contrast* effect [3], is useful and important in many biomedical applications.

Thus, given the special characteristics of SR-μCT and the possibilities of the current third generation SR facilities, especially regarding their application in medicine and biology, image processing algorithms applied to SR-μCT segmentation are currently investigated. Traditional segmentation methods such as thresholding, possibly aided by morphological filters, may be highly sensitive to small parameter changes, and may cause loss of details; both phenomena are not desirable for analysis and/or quantification, and we also provide results that in fact corroborate this statement, showing that conventional methods based on thresholding and linear/nonlinear filtering do not cope with phase contrast intensity variation. In addition, the presence of a large number of 2D images (approximately 500 or 600 slices) in each SR-μCT scan, with also the large number of scans should be performed in biomedical research, would make the manual

* Corresponding author. Tel.: +55 21 2334 0725.
E-mail address: ameneses@ieee.org (A.A.M. Meneses).

0168-9002/
doi:10.1016/j.nima.2011.08.007

segmentation impractical, which leads the researches toward automated segmentation methods that cope with phase contrast intensity variation. Therefore, investigation on the application of state-of-the-art segmentation methods to μCT is an important research topic, due to the interesting characteristics and applications of that imaging modality.

As examples of the application of novel approaches to CT images, Krebs et al. [4] describe the segmentation of high resolution CT images using fuzzy approaches [5] for the assessment of trabecular distances. Meneses et al. [6,7] reported the application of Artificial Neural Networks (ANNs) [8,9] to the segmentation of SR-μCT biomedical images, and the proposal and the assessment of ANNs training strategies for segmentation with respect to SR-μCT bone images for histomorphometry applications [10].

Since the μCT imaging modality is only at its beginning [11], algorithms that yield high-quality results shall also be investigated and assessed. One of those state-of-the-art algorithms that yield remarkable results is the min-cut/max-flow algorithm [12–15], used for segmentation based on energy minimization. The energy minimization problem is relevant in many computer vision areas. As an example in medical imaging, Schneider et al. [16] use the min-cut/max-flow algorithm for energy minimization in their *annulus segmentation algorithm* for ultrasound imaging. The contributions of Boykov et al. [13], especially regarding the swap move and expansion move algorithms, represent a breakthrough in image segmentation research, yielding fast and accurate results in many image processing fields. For simplicity, we refer to the application of the min-cut/max-flow swap move algorithm for the minimization of energy as Energy Minimization via Graph Cuts (EMvGC).

For SR-μCT images, in the case of bone tissue segmentation, the results of EMvGC almost perfectly overlap manual segmentation, as expected and as we will discuss later. As an example of application, Fig. 1 depicts the 3D visualization of the sample E8D; Fig. 2 depicts the slice no. 305 (with normalization, the effects of the phase contrast effect become more pronounced). In Fig. 2, there exist basically three regions: bone, marrow (surrounded by the bony tissue region), and cartilage (outside the bone; seen in Fig. 1 as a sort of halo surrounding the bone).

For other types of images, such as those of biological soft tissues, phase contrast effects allow a better visualization of structures. Phase contrast effects cause variation in the intensity

Fig. 1. Three-dimensional visualization of dorsal portion of Wistar rat rib bone (sample E8D).

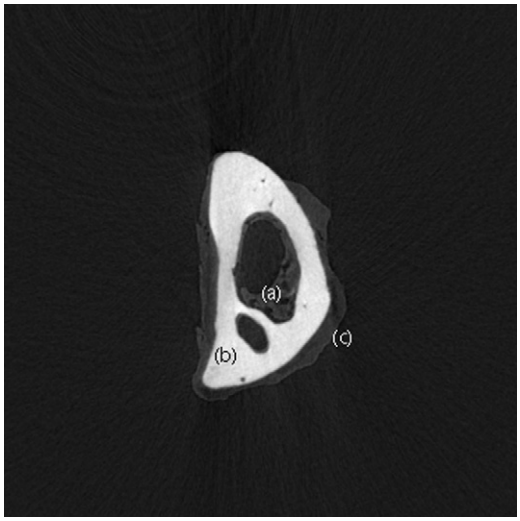

Fig. 2. Slice 305 of Wistar rat rib (bone from the dorsal portion; sample E8D): (a) marrow; (b) bone and (c) cartilage.

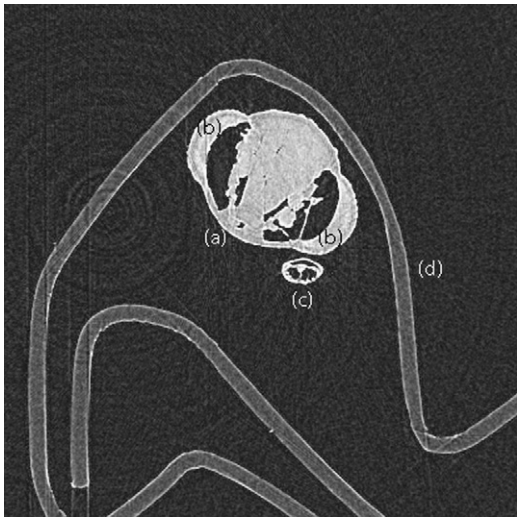

Fig. 3. Slice 183 of the insect *Rhodnius prolixus* (sample C4B): (a) head; (b) eyes; (c) proboscis (which was beside the body due to the preparation of the sample) and (d) plastic used in order to fasten the sample on the experimental setup.

at the edges of an object or region, basic characteristic for their great potential for analysis and visualization of biological microstructure [17,18]. In those cases, such as represented in Fig. 3, one slice of the μCT of the insect *Rhodnius prolixus* (also known as *kissing bug*), vector of the Chagas's disease (slice no. 183, sample C4B), the area of interest (light gray) has an intensity similar to the intermediate gray region (plastic used in order to fasten the sample on the experimental setup), or the insect's inner structures may have similar intensities. Notice the variation of intensity at the edges of the regions, with darker pixels in the background and lighter pixels on the insect's body and plastic regions.

Scans of bone samples, as the one depicted in Fig. 1, are relatively less complex for segmentation due to the contrast between the region of interest (bone) and the rest of the image. On the other hand, images such as the μCT scans of *Rhodnius prolixus* are more complex due to phase contrast effects, summed to the lack of contrast between regions, which in fact cause misclassifications during the segmentation performed by the EMvGC algorithm. Nevertheless it is possible to correct the results

yielded by the EMvGC with ANNs trained with context information about misclassified pixels, in order to solve this issue, as we will demonstrate later. Hence, the characteristics of fast and accurate segmentation of the EMvGC algorithms may be used despite the complexity of such images. Therefore, the techniques EMvGC and EMANNs cope with the task of performing segmentation in images with the intensity variation due to phase contrast effects, presenting a superior performance in comparison to results yielded by conventional segmentation techniques based on thresholding and linear/nonlinear image filtering, which are also presented in the present article.

Conventional segmentation techniques such as thresholding and linear/nonlinear image filtering are not able to cope with the intensity variation caused by phase contrast effects (see Table 3, columns T and TF). In the case of insect SR-μCT scans, with those conventional techniques, it becomes impossible to segment accurately the area of interest (insect region), that is, whenever conventional techniques are used, pixels outside the insect (for example, the light gray pixels in the borders of the plastic region that present pixel intensity similar to the insect region) will be labeled in the segmentation process as if they belonged to the insect region, causing mis-segmentation. The automated methods described in the present article are able to perform the segmentation despite the intensity variation that conventional techniques such as the ones mentioned do not attain. Once the region of interest is segmented correctly, it is possible to subtract the regions that are not interesting from the scans without impairing the original quality of the region of interest, preserving the phase contrast effects with minimal loss of information.

In short, since μCT is an imaging modality with a wide range of applications as well as an enormous potential in biomedicine, the study and assessment of image processing techniques is needed, taking into account its specificities as the phase contrast effects, since they are helpful and sometimes indispensable in many applications and analyses. Therefore, the contributions of the present work are (i) the assessment and the discussion of the application of the EMvGC algorithm [12–14], to SR-μCT images concerning biomedical applications, and (ii) a method consisting in the use of the EMvGC algorithm with Artificial Neural Networks (trained with context information related to pixel intensity) for avoiding the misclassification of pixels due to phase contrast effects (that is, pixels that present intensity similar to the region of interest and are therefore mis-segmented). The methods described allow a correct segmentation and preserve the phase contrast effects where they are interesting, that is, in regions of interest, without impairing the information provided in the original image.

The rest of this article is organized as follows. The materials and methods are described in Section 2. The results of simple image processing techniques are described in Section 3. The results yielded by EMvGC and EMANN are presented in Section 4. In Section 5, we discuss the results, and finally the conclusion is presented in Section 6.

2. Materials and methods

2.1. Biomedical samples and characteristics of the images

A total of eleven biomedical samples were used in the present work, divided in two groups. The first group encompasses samples of four Wistar rats rib (dorsal bone portion), labeled as E8D, F6D, F7D, and F8D. The second group contains seven of the insect *Rhodnius prolixus*, labeled as C3B, A3B, C4B, A4B, C10B, A10B, and JB. All the specimens are the object of current biological research, prepared according to standard biological procedures.

Table 1
Dimensions and number of slices of μCT volumes.

Sample	Dimensions (in pixels^2)	Number of slices
E8D	240×240	579
F6D	544×544	580
F7D	544×544	580
F8D	495×495	580
C3B	312×312	585
A3B	395×395	507
C4B	412×412	560
A4B	379×379	585
C10B	443×443	500
A10B	394×394	507
JB	324×324	540

The dimensions and the number of slices of the images are given in Table 1 (some of them were re-dimensioned in order to eliminate unnecessary background region).

Figs. 2 and 3 are the examples of slices given by the reconstruction software, provided by the Elettra Laboratory. The general characteristics of the images include, for the first group, a high contrast between the bone region and marrow and cartilage regions, as depicted in Fig. 2; for the second group, low contrast between the insect region (light gray) and the plastic region (intermediate gray), as depicted in Fig. 3. Such different characteristics were interesting for the verification of robustness of the algorithms tested.

2.2. Synchrotron radiation micro-Computed Tomography

The images of interest were obtained at the Synchrotron Radiation for Medical Physics (SYRMEP) beam line at the Elettra Laboratory (Trieste, Italy—www.elettra.trieste.it).

The aforementioned beam line is designed for *in-vitro* samples X-ray imaging, and provides important characteristics for the acquisition of medical images, such as a extremely collimated laminar beam. SR beams are, to a good extent, coherent, allowing higher sensitivity and better spatial resolution, which provides images with richness in details, to be a factor for the development imaging techniques. Moreover, the high brilliance of the synchrotron light allows the use of monochromatic radiation, i.e. the selection of single photon energy. Monochromaticity avoids beam hardening and therefore turns a reconstructed radiography in a quantitative mapping of X-ray attenuations. In addition SR phase contrast imaging provides enhanced image quality, compared to conventional absorption X-ray imaging [17].

SYRMEP beam line provides a monochromatic laminar-section X-ray with a maximum area of about 160×5 mm^2 at 20 keV, at a distance of about 23 m from the source. The system consists of a Si (1 1 1) crystal working at the Bragg configuration. The useful energy range is $8-35$ keV. The intrinsic energy resolution of the monochromator is about 10^{-3}. Typical flux measured at the sample position at 17 keV is about 1.6×10^8 photons/mm^2 s with a stored electron beam of 300 mA as ELETTRA operates at 2 GeV [19]. A custom-built ionization chamber is placed upstream to the sample to determine the exposure on the sample. A micrometric vertical and horizontal translation stage allows the positioning and the scanning of the sample with respect to the stationary beam and a rotational stage allows CT acquisition with a resolution of 0.001°.

The detector system is a water-cooled CCD camera (Photonics Science XDIVHR), a 12/16 bit, 4008×2672 full frame, 4.5-micron pixel size CCD camera with a field of view of 18×12 mm^2. It is coupled to a Gadox scintillator placed on a straight fiber optics coupler. The CCD camera moves along the sample – detector axis,

in order to set the desired sample-to-detector distance d. According to the choice of the sample-to-detector distance, one may distinguish between the absorption and phase sensitive regimes. If the CCD is mounted very close to the sample we are in the absorption regime. For higher d values, free space propagation transforms the phase modulation of the transmitted beam into an amplitude modulation.

2.3. Phase contrast imaging

The information carried by the phase of X-ray wavefield, or *phase effects*, may have converted it into image contrast, enhancing detail visibility [3], especially if compared to the poor contrast given by media with small X-ray absorption differences [19]. In other words, phase contrast imaging allows the visualization of objects that have very similar X-ray absorption properties.

According to Lewis [17], the three experimental techniques used to obtain images with contrast enhancement based on phase-shift effects are X-ray interferometry, Diffraction Enhanced Imaging and in-line holography. The latter is also known as free-space propagation or merely *phase contrast* imaging [20–24].

In phase contrast imaging, details refract X-ray waves, which interfere with unrefracted ones, resulting in strong interference patterns at the borders of certain regions or objects, detected by the instrumentation [19]. Such phenomenon occurs in regions with abrupt changes in the refraction index. The effect of the phase contrast may be noticed slightly in Fig. 2 (at the edges of marrow and cartilage regions) and more significantly in Fig. 3 (at the borders of plastic and insect regions). Phase contrast imaging exploits differences in the real part of the refractive index distribution of an object to form an image using a spatially coherent light source. For a more detailed discussion on phase contrast imaging and images comparing X-ray absorption and phase contrast imaging, the interested reader may refer to [17].

2.4. Simple segmentation techniques

As different regions to be segmented are characterized by different intensity levels, a natural attempt at segmentation consists of the application of common image processing techniques based on thresholding and linear/nonlinear image filtering.

In order to assess the separability of the different regions via thresholding, histograms of pixel values corresponding to the three regions of interest can be plotted (Fig. 4); as the three histograms significantly overlap (mostly due to phase contrast effects and – to a lesser degree – due to noise), one cannot expect good results when using thresholding alone, even when thresholds are set to the optimal values.

A commonly implemented countermeasure is to preprocess the image by performing lowpass filtering, which reduces noise but loses details at edges, and/or using nonlinear, edge-preserving filters such as a median filter. In the current context, the experimental results reported in Section 3 show that these techniques, while beneficial, are not effective enough to obtain satisfactory results, and would not allow one to perform accurate measurements or obtain good-quality 3D visualizations.

The following sections describe more sophisticated segmentation techniques, which effectively overcome such problems.

2.5. Energy minimization via Graph Cuts

2.5.1. Energy minimization

In computer vision, many tasks that involve the assignment of a label to pixels are naturally stated in terms of energy minimization. Using the notation in Ref. [13], a piecewise smooth labeling f consistent with the observed data is sought, in order to minimize the energy function. According to f, a label $f_p \in \mathscr{L}$, where $\mathscr{L}$ is a finite set of labels, is assigned to each pixel $p \in \mathcal{P}$. The energy functions $E(f)$ considered for minimization via Graph Cuts [13] are of the following form:

$$E(f) = \sum_{\{p,q\} \in \mathcal{N}} V_{p,q}(f_p, f_q) + \sum_{p \in \mathcal{P}} D_p(f_p) \quad (1)$$

The function $D_p(f_p)$ typically corresponds to $(f_p - I_p)^2$ and measures the disagreement between f_p and the observed intensity I_p for each pixel p. The function $V_{p,q}(f_p, f_q)$ computes the cost of assigning f_p and f_q to the pair of pixels $\{p, q\} \in \mathcal{N}$, where the set $\mathcal{N}$ often comprises adjacent pixels, although not necessarily. During the evaluation of $E(f)$, relatively high values of $V_{p,q}$ indicate that f does not correspond to a piecewise smooth labeling.

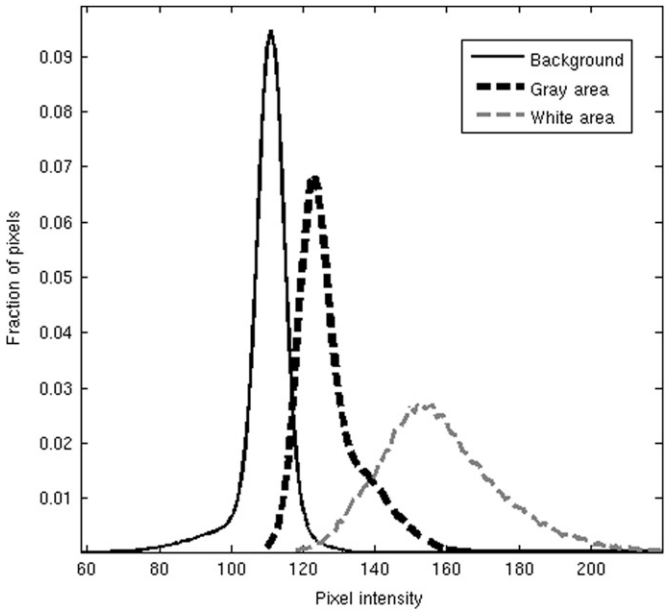

Fig. 4. Histograms corresponding to pixel intensity values associated to the background, gray (plastic) and white (insect) regions in sample A10B. As the histograms significantly overlap, the regions are not easily separable by simple thresholding even if optimal thresholds are set.

2.5.2. Graph Cuts

Min-cut/max-flow optimization problems [25] may be formulated as follows. Given a weighted graph $\mathcal{G}\langle \mathcal{V}, \mathcal{E} \rangle$, where $\mathcal{V}$ is a collection of nodes (or vertices) connected by a collection of edges $\mathcal{E}$, with two distinguishable nodes called terminals (or source and sink), the minimum cut problem is to find the cut $\mathcal{C} \subset \mathcal{E}$ that separates the terminal nodes, with minimum cost. The cost of the cut $|\mathcal{C}|$ corresponds to the sum of its edge weights. Ford and Fulkerson [26] proved that the minimum cut problem is equivalent to the problem of the maximum flow between the terminals.

Boykov et al. [13] proposed two algorithms for multidimensional energy minimization, achieving approximate solutions with guaranteed optimality bounds: the swap move algorithm and the expansion move algorithm. Unlike other algorithms such as Simulated Annealing, these algorithms provide solutions in a nearly linear time in practice [13]. The library used in our implementations (gco-v3.0) is available for research purposes at http://vision.csd.uwo.ca/code/. In our implementations, the EMvGC considered 3D information, that is, besides the bi-dimensional information contained at each slice, the information of adjacent slices was also considered during the execution of the algorithm.

In medical imaging, one recent application based on the use of the min-cut/max-flow algorithm was proposed by Schneider et al. [16], for segmentation of mitral annulus in 3D ultrasound images.

2.6. Artificial neural networks

Neural Computing is a part of the Computational Intelligence that represents models inspired by the brain. Such models are based on the relationships among neurons, synapses and learning, since the brain is a "highly complex, non-linear and parallel" computer [8]. ANNs execute tasks such as regression, pattern recognition and classification. Egmont-Petersen et al. [9] reviewed the application of ANNs to image processing. The usage of ANNs is interesting due to its attractive characteristics for pattern recognition and classification, unlike conventional techniques such as morphological filtering and binarization.

Meneses et al. [6,7,10] applied ANNs to SR-μCT biomedical images for the classification of bone pixels for histomorphometric analysis. Their basic approach was the use of the intensity of pixels as inputs for the training phase. In [10], the authors presented training strategies that combined algorithms and information about the symmetry of the patterns. According to [10], ANNs provided considerable results in the validation, with a satisfactory segmentation of cortical bone μCT slices.

However, in the present work, the information used during the ANNs' training phase was different. In this case, we were interested in the usage of context information about misclassified pixels that did not belong to a certain region. Based on the image of Fig. 3, as well as the image resultant from the application of the EMvGC algorithm (Fig. 7), it was possible to gather statistical information such as the mean intensity of pixels and its standard deviation (within a kernel with dimensions 11×11 pixels^2) for both the normalized and the image segmented by EMvGC. Besides, with the image segmented, it was possible to create another binarized image only with background and the plastic region, and the fifth input was composed by the average within the aforementioned kernel (this input is related to the proximity of the pixel of interest to plastic regions). Thus, the ANNs had basically those five input patterns (mean and standard deviation for the normalized image; mean and standard deviation for the image segmented by EMvGC; and the mean related to a binarized image, containing only background and the plastic region), with a training set composed by 50 target central pixels selected and previously classified by two of the authors (A.A.M.M. and A.P.A.), yielding as outputs 0 for "plastic border" white pixel or 1 for "insect" white pixel. The Levenberg–Marquardt algorithm was used in the training phase [27]. The stopping criterion was set to 10000 epochs or an MSE for the training phase lower than 10^{-10}.

2.7. Dice Similarity Coefficient

The Dice Similarity Coefficient (DSC) [28] between two sets A and B is a spatial overlap index given by

$$DSC(A,B)=\frac{2n(A\cap B)}{n(A)+n(B)} \quad (2)$$

where $n(\cdot)$ is the number of elements of a set. The original usage of the *DSC* in ecologic association considered S_1 and S_2 as sets of species within a given region. Thus, DSC could be used as an index regarding ecological relationship between species. The *DSC* ranges from 0 (no overlap) to 1 (complete overlap).

The application of *DSC* is straightforward in image segmentation. Given an image, consider the n sets of pixels A_1, A_2, …, A_n (i.e., with the labels $i=1,2,\ldots,n$) corresponding to distinct objects or regions of the image, in our case obtained by manual segmentation (the ground truth). If the same image is submitted to another process of segmentation, the automated segmentation provided by the techniques EMvGC or EMANN, and the sets of pixels B_1, $B_2,\ldots,B_n$ are yielded, then it is possible to compare the spatial overlap of each region A_i with the corresponding set B_i.

Zijdenbos et al. [29] proposed a method for segmentation of magnetic resonance images and used the *DSC* for validation, demonstrating that the *DSC* is a special case of the kappa statistic. Zou et al. [30] also discussed the statistical validation of magnetic resonance imaging segmentation based on the *DSC*. Gupta et al. [31] used the *DSC* for comparison of CT images segmentation. The well-known Jaccard coefficient (J) [32], also used for the evaluation of image segmentation, and the *DSC* are related by the equation $DSC=2J/(J+1)$.

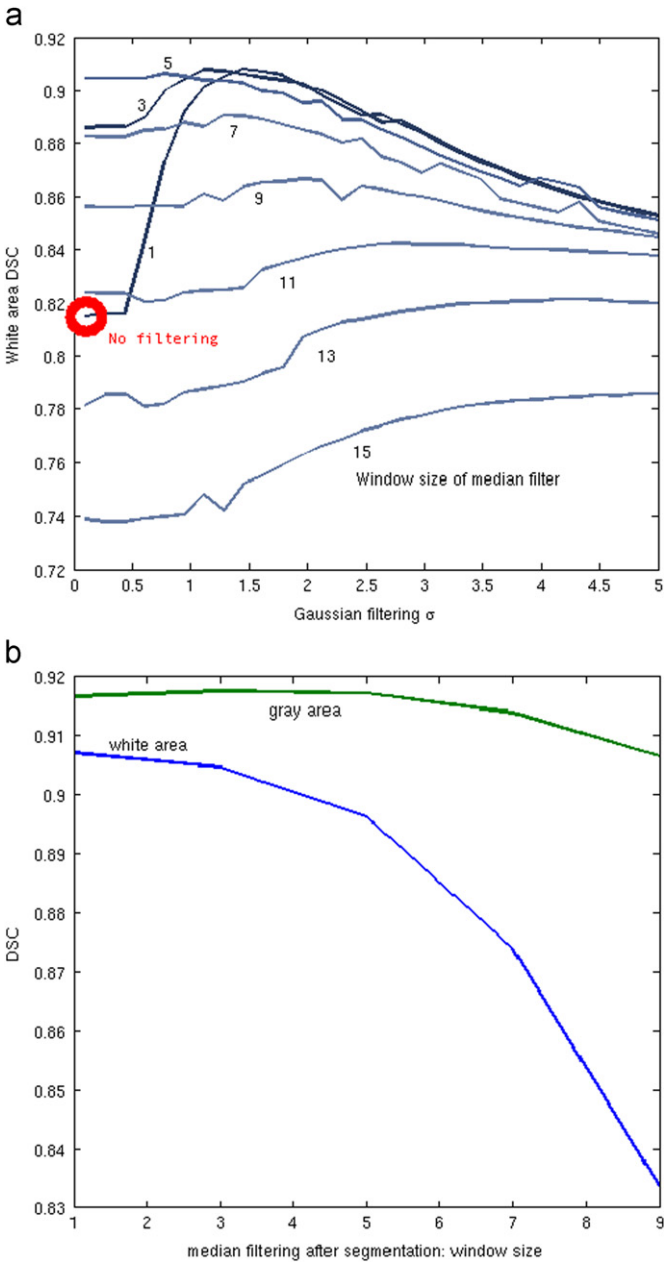

Fig. 5. Effects of filtering parameters on the performance of thresholding with filtering (TF) on sample A108. (a) Effect of Gaussian smoothing parameter σ (x axis) on white region segmentation performance (y axis); the curve is reported for several values for the W_{mf} parameter, and $W_{mfp}=1$. The case with no filtering (T), i.e. $\sigma=0$, $W_{mf}=1$, $W_{mfp}=1$, is marked by a circle. (b) Effect of different values for regularization parameter W_{mfp} (x axis) on segmentation performance for the white and gray regions.

3. Results of simple image processing techniques

In order to determine the improvements of the proposed techniques over standard approaches, in the following we report upper bounds on *DSC* results obtainable using simple thresholding (*T*), and thresholding after image filtering (TF), in addition to the results obtained using the proposed EMvGC and EMANN techniques. In particular, *T* values are computed using the optimal thresholds, i.e. the thresholds that lead to the minimal misclassification rate for any given image; this provides an upper bound to the performance obtainable using such technique. For obtaining TF performance values, we implemented the following procedure:

- the input image is smoothed with a Gaussian lowpass filter with a given parameter σ, representing the gaussian variance;
- the image is filtered using a nonlinear median filter with a given window size W_{mf} ;
- the optimal thresholds are computed and the image is segmented by thresholding and
- the segmentation results are regularized using a median filter with a given window size W_{pmf} ;

The procedure is repeated for all possible combinations of several realistic possibilities for the three values σ, W_{mf} and W_{pmf}, and the best result is taken as the upper bound for the obtainable performance and reported in Tables 3 and 4. Experiments have also been performed using other morphological filters in place of a median filter (i.e. binary opening, binary closure), with slightly inferior results. Fig. 5 depicts the effects of different parameters on TF performance for one of the insect samples.

4. Results

Figs. 6 and 7 represent examples of the application of the EMvGC to the images in Figs. 2 and 3, respectively. Notice that, in Fig. 7, although the EMvGC algorithm is accurate for the insect region, phase contrast effects in the edges of the plastic region lead to a misclassification of the edges. Fig. 8 depicts the result of the application of the EMANN technique, that is, the application of ANNs (after the EMvGC algorithm) in order to correct misclassified white pixels according to pattern and context information, as discussed previously. The pattern recognition of white pixels that belong to the plastic region was successful due to context

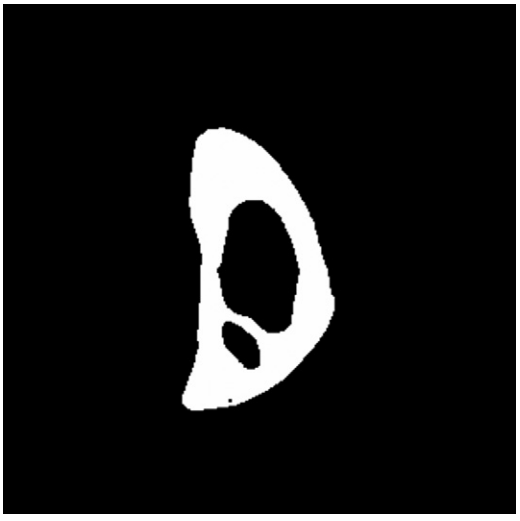

Fig. 6. Result of the application of the EMvGC algorithm to the slice depicted in Fig. 2.

Fig. 7. Result of the application of the EMvGC algorithm to the slice depicted in Fig. 3. When only the algorithm EMvGC is applied, plastic borders are segmented in white due to phase contrast intensity variation, although they are not of biological interest.

Fig. 8. Result of the application of the EMANN technique to the slice depicted in Fig. 3. With this method, it was possible to segment in white only the area of biological interest. Thus, context information of pixel intensities may be used by pattern recognition methods in order to cope with pixel intensity variation due to phase contrast effects.

statistical information used during the ANN's training phase. Fig. 9 exhibits enlarged ROIs for the insect scan results.

Table 2 exhibits the *DSC* related to the application of the technique EMvGC to the rat ribs SR-μCT volumes (white region/bone). Tables 3 and 4 exhibit the *DSC* related to the application of EMvGC and EMANN to the *Rhodnius prolixus* SR-μCT volumes (gray region/plastic and white region/insect, respectively). Figs. 10 and 11 depict the numerical results related to Tables 3 and 4 regarding EMvGC and EMANN. The logit transformation was used in order to perform the statistical analysis according to [30,33]; the bars represent a confidence interval of the mean at level 95% for each sample, using the Student's *t* distribution ($n=10$).

5. Discussion

Accurate segmentation processes may provide accurate quantification methods to assess effects of either diseases or drugs.

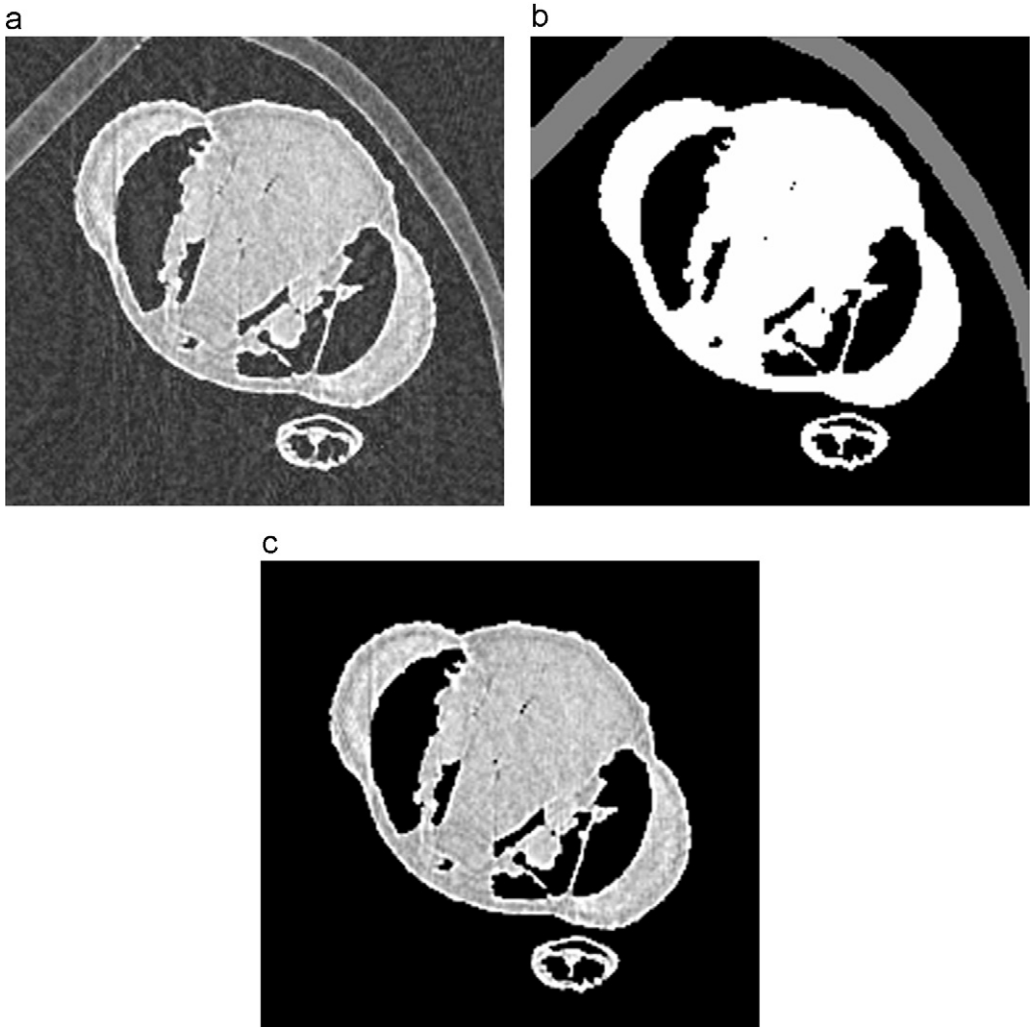

Fig. 9. (a) Enlarged image with the ROI related to the image depicted in Fig. 3; (b) result of the segmentation by the method EMANN; (c) detail of the image obtained with the subtraction of not interesting regions (in this case, background and plastic regions), which is used for renderization. Pixels in light gray (in the plastic region) that did not belong to the regions of interest (in the insect) were correctly segmented due to the classification provided by the method EMANN. The effects inside the region of interest is minimal although its pixels have intensity similar to pixels that belong to regions that were to be excluded, preserving the characteristics of phase contrast effects, interesting for analysis of those images.

Table 2
DSC values for the white region (bone)—results of the application of EMvGC to Wistar rat ribs μCT volumes.

Sample	EMvGC (%)
E8D	99.94
F6D	99.82
F7D	99.90
F8D	99.85
Mean	**99.88**

Table 3
DSC values for the gray region (plastic)—reslts of the application of simple thresholding (*T*), thresholding after image filtering (TF), EMvGC and EMANN to *Rhodnius prolixus* μCT volumes.

Sample	*T* (%)	TF (%)	EMvGC (%)	EMANN (%)
C3B	77.62	91.05	91.64	97.97
A3B	71.65	90.83	89.68	99.74
C4B	79.66	93.17	90.36	98.97
A4B	79.40	92.96	89.19	98.68
C10B	72.04	93.32	89.30	99.25
A10B	77.79	93.45	87.06	99.53
JB	91.63	92.52	96.30	98.50
Mean	**78.54**	**92.47**	**90.50**	**98.95**

As exhibited in Table 2, the application of the EMvGC algorithm to the segmentation of Wistar rat rib samples SR-μCT images attain in average 99.88%, which indicates a successful application of the EMvGC algorithm.

Nevertheless, the phase contrast effects in SR-μCT images, important and sometimes indispensable for visualization and analysis, may impair the performance of the EMvGC algorithm (see Fig. 7 for a visual example of mis-segmentation in the *Rhodnius prolixus* samples SR-μCT images; and the *DSCs* 90.50% and 77.68%, in average for EMvGC, exhibited in Tables 3 and 4), since the borders of the plastic region have their intensity increased by those effects.

In order to correct the misclassification provided by EMvGC, we used ANNs trained with information concerning statistical data for the classification of those pixels, characterizing the technique EMANN. With this approach, it was possible to increase the *DSCs*, resulting in 98.95% and 98.02% in average for the *Rhodnius prolixus* images (an increase of approximately 8.45% and 20.34%, respectively).

Table 4
DSC values for the white region (insect) – results of the application of simple thresholding (*T*), thresholding after image filtering (TF), EMvGC and EMANN to *Rhodnius prolixus* μCT volumes.

Sample	*T* (%)	TF (%)	EMvGC (%)	EMANN (%)
C3B	79.20	85.82	75.63	97.22
A3B	79.35	83.96	81.58	99.72
C4B	85.32	93.16	72.90	97.32
A4B	79.93	88.28	75.53	96.19
C10B	82.11	91.76	80.05	98.85
A10B	75.55	90.76	68.11	98.92
JB	93.35	93.31	89.97	97.93
Mean	**82.12**	**89.58**	**77.68**	**98.02**

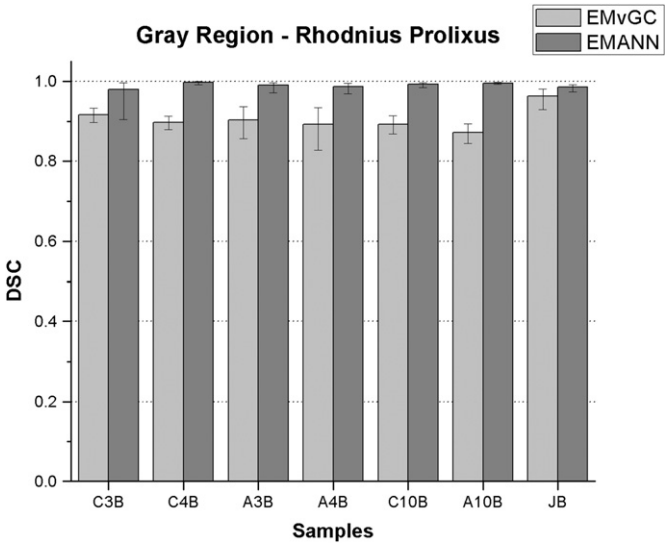

Fig. 10. Column plot for the *DSC* of gray pixels for the samples of the *Rhodnius prolixus*. The best results for all samples were obtained with the technique EMANN.

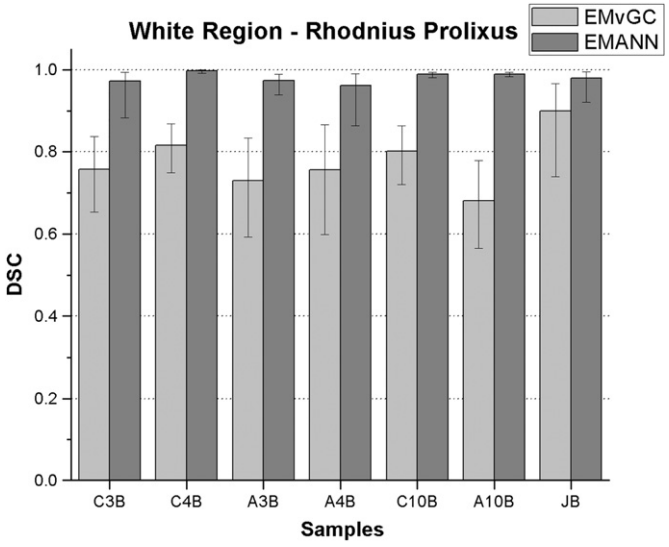

Fig. 11. Column plot for the DSC of white pixels for the samples of *Rhodnius prolixus*. The best results for all samples were obtained with the technique EMANN.

In short, the application of the EMvGC and EMANN techniques attained remarkable performance for SR-μCT images. The misclassifications due to phase constrast effects were readily corrected, with ANNs trained with statistical data representing context information. The final 3D visualization is depicted in Figs. 12 and 13. After the segmentation, the pixels of the regions of interest were substituted for the pixels of correspondent normalized images. Visualization is made possible by segmenting each slice, and rendering the volume associated to the areas of interest.

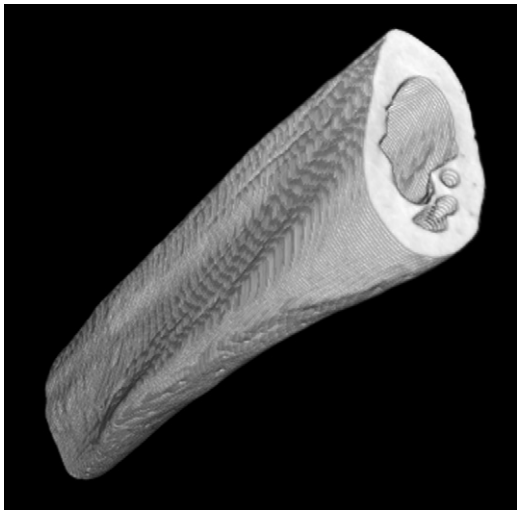

Fig. 12. Three-dimensinoal visualization of dorsal portion of Wistar rat rib bone (sample E8D) after the segmentation with EMvGC.

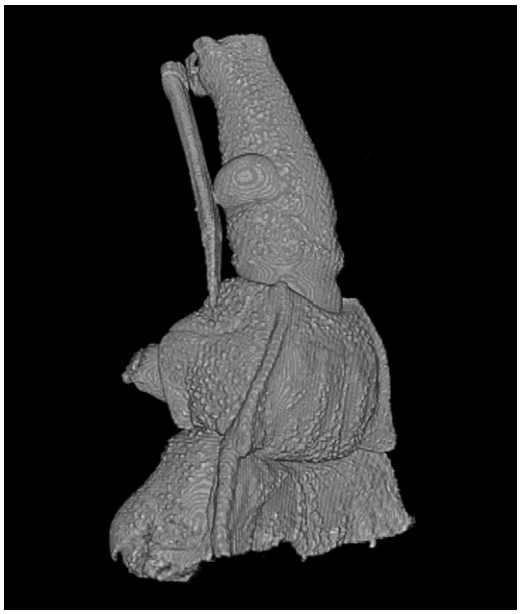

Fig. 13. Three-dimensional visualization of a *Rhodnius Prolixus* insect (sample C4B) after the segmentation with EMANN (proboscis, head, prothorax and part of the mesothorax—areas of interest of current research).

6. Conclusion

The present article reports the application of EMvGC algorithm to SR-μCT biomedical images. EMvGC is a state-of-art algorithm which is fast and accurate, with many applications in computer vision. Since its application to segmentation of images obtained by SR-μCT needed analysis and assessment, we presented its

outcomes in the segmentation of Wistar rat ribs and *Rhodnius prolixus* insect samples images (Chagas's disease vector), based on the *DSC*, which is a measure of spatial overlap. For Wistar rat ribs scans, the EMvGC algorithm the *DSC* reached in average 99.88%.

Although phase contrast effects are highly desirable by researchers for the visualization and the analysis of biomedical images, they cause high intensity in pixels of edge regions, resulting in misclassification of pixels performed by the EMvGC algorithm. In order to overcome this issue, we proposed the joint method EMANN, in which, after a previous segmentation done by the EMvGC algorithm, an ANN is trained with statistical data, representing context information about the region where the pixels belong. With the EMANN technique, the issues about misclassification of high intensity pixels due to phase contrast effects have been solved, reaching *DSCs* such as 98.95% and 98.02% in average. With this method, it was possible to segment in white only the areas of biological interest. Thus, context information of pixel intensities may be used by pattern recognition methods in order cope with pixel intensity variation due to phase contrast effects. Futhermore, both EMvGC and EMANN performed better than conventional techniques such as thresholding and linear/nonlinear filtering for bone and insect imaging, respectively.

Acknowledgment

The authors thank the researchers Patrícia Azambuja (Laboratory of Physiology and Biochemistry of Insects, Instituto Oswaldo Cruz) and Marcelo S. González (Laboratory of Biology of Insects) for insect samples and technical discussions, as well as the SYRMEP beam line staff for the support. A.A.M.M. acknowledges the Brazilian agencies CAPES and FAPERJ (Grant E-26/102.493/2010). R.C.B. acknowledges the partial financial support from the Abdus Salam International Centre for Theoretical Physics (ICTP, Trieste, Italy) through the Associate Scheme. A.P.A. thanks the agency CNPq for financial support. The authors would like to thank the reviewers for their valuable comments and suggestions.

References

[1] F.R. Elder, A.M. Gurewitsch, R.V. Langmuir, H.C. Pollock, Phys. Rev. 71 (1947) 829.
[2] G.N. Hounsfield, Br. J. Radiol. 46 (1973) 1016.
[3] A. Olivo, Nucl. Instr. and Meth. A 548 (2005) 194.
[4] A. Krebs, C. Graeff, I. Frieling, B. Kurz, W. Timm, K. Engelke, C.-C. Glüer, Bone 44 (2009) 145.
[5] L.A. Zadeh, Computer 21 (1988) 83.
[6] A.A.M. Meneses, C.J.G. Pinheiro, R. Schirru, R.C. Barroso, D. Braz, L.F. Oliveira, IEEE Nucl. Sci. Symp. Med. Imaging Conf. Rec. (2008) 5309.
[7] A.A.M. Meneses, C.J.G. Pinheiro, L.M. Gambardella, R. Schirru, R.C. Barroso, D. Braz, L.F. Oliveira, IEEE Nucl. Sci. Symp. Med. Imaging Conf. Rec. (2009) 3437.
[8] S. Haykin, Neural Networks: A Comprehensive Foundation, Pearson Education, 2005.
[9] M. Egmont-Petersen, D. de Ridder, H. Handels, Pattern Recognition 35 (2002) 2279.
[10] A.A.M. Meneses, C.J.G. Pinheiro, P. Rancoita, T. Schaul, L.M. Gambardella, R. Schirru, R.C. Barroso, L.F. Oliveira, Nucl. Instr. and Meth. A 621 (2010) 662.
[11] D. Chappard, M.-F. Baslé, E. Legrand, M. Audran, Morphologie 92 (2008) 162.
[12] D.M. Greig, B.T. Porteous, A.H. Seheult, J. R. Stat. Soc. B 51 (1989) 271.
[13] Y. Boykov, O. Veksler, R. Zabih, IEEE Trans. Pattern Anal. Mach. Intell. 23 (2001) 1222.
[14] V. Kolmogorov, R. Zabih, IEEE Trans. Pattern Anal. Mach. Intell. 26 (2004) 147.
[15] Y. Boykov, V. Kolmogorov, IEEE Trans. Pattern Anal. Mach. Intell. 26 (2004) 1124.
[16] R.J. Schneider, D.P. Perrin, N.V. Vasilyev, G.R. Max, P.J. del Nido, R.D. Howe, IEEE Trans. Med. Imaging 29 (2010) 1676.
[17] R.A. Lewis, Phys. Med. Biol. 49 (2004) 3573.
[18] O. Betz, U. Wegst, D. Weide, M. Heethoff, L. Helfen, W.-K. Lee, P. Cloetens, J. Microsc. 227 (2007) 51.
[19] F. Arfelli, et al., Radiology 215 (2000) 286.
[20] A. Snigirev, I. Snigireva, V. Kohn, S. Kuznetsov, Rev. Sci.Instrum. 66 (1995) 5486.
[21] U. Bonse, F. Busch, Prog. Biophys. Mol. Biol. 65 (1996) 133.
[22] P. Cloetens, R. Barrett, J. Baruchel, J.-P. Guigay, M. Schlenker, J. Phys. D 29 (1996) 133.
[23] A.V. Bronnikov, J. Opt. Soc. Am. A 19 (2002) 472.
[24] T. Weitkamp, D. Haas, D. Wegrzynek, A. Rack, J. Synch. Rad. 18 (2011) 617.
[25] R.K. Ahuja, T.L. Magnanti, J.B. Orlin, Network Flows: Theory, Algorithms and Applications, Prentice-Hall, 1993.
[26] L. Ford, D. Fulkerson, Flows in Networks, Princeton University Press, 1962.
[27] H. Demuth, M. Beale, Neural Network Toolbox, The MathWorks, 2004.
[28] L.R. Dice, Ecology 26 (1945) 297.
[29] A.P. Zijdenbos, B.M. Dawant, R.A. Margolin, A.C. Palmer, IEEE Trans. Med. Imaging 13 (1994) 716.
[30] K.H. Zou, S.K. Warfield, A. Bharatha, C.M.C. Tempany, M.R. Kaus, S.J. Haker, W.M. Wells III, F.A. Jolesz, R. Kikinis, Acad. Radiol. 11 (2004) 178.
[31] V. Gupta, W. Ambrosius, G. Qian, A. Blazejewska, R. Kazmiersky, A. Urbanik, W.L. Nowinsky, Acad. Radiol. 17 (2010) 1350.
[32] P. Jaccard, Bull. Soc. Vaudoise Sci. Nat. 37 (1901) 241.
[33] A. Agresti, Categorical Data Analysis, John Wiley & Sons, 1990.